TU Delft

Delft University of Technology

Effects of high-amplitude low-frequency structural vibrations and machinery sound waves on ultrasonic guided wave propagation for health monitoring of composite aircraft primary structures

Ochôa, Pedro A.; Groves, Roger M.; Benedictus, Rinze

DOI
10.1016/j.jsv.2020.115289

Publication date
2020

Document Version
Final published version

Published in
Journal of Sound and Vibration

Citation (APA)
Ochôa, P. A., Groves, R. M., & Benedictus, R. (2020). Effects of high-amplitude low-frequency structural vibrations and machinery sound waves on ultrasonic guided wave propagation for health monitoring of composite aircraft primary structures. *Journal of Sound and Vibration*, *475*, Article 115289. https://doi.org/10.1016/j.jsv.2020.115289

Important note
To cite this publication, please use the final published version (if applicable).
Please check the document version above.

Copyright
Other than for strictly personal use, it is not permitted to download, forward or distribute the text or part of it, without the consent of the author(s) and/or copyright holder(s), unless the work is under an open content license such as Creative Commons.

Takedown policy
Please contact us and provide details if you believe this document breaches copyrights.
We will remove access to the work immediately and investigate your claim.

This work is downloaded from Delft University of Technology.
For technical reasons the number of authors shown on this cover page is limited to a maximum of 10.

Journal of Sound and Vibration 475 (2020) 115289

Contents lists available at ScienceDirect

Journal of Sound and Vibration

journal homepage: www.elsevier.com/locate/jsvi

Effects of high-amplitude low-frequency structural vibrations and machinery sound waves on ultrasonic guided wave propagation for health monitoring of composite aircraft primary structures

Pedro A. Ochôa [a, b, *], Roger M. Groves [b], Rinze Benedictus [a]

[a] Structural Integrity and Composites Group, Faculty of Aerospace Engineering, Delft University of Technology, the Netherlands
[b] Aerospace Non-Destructive Testing Laboratory, Faculty of Aerospace Engineering, Delft University of Technology, the Netherlands

ARTICLE INFO

Article history:
Received 2 September 2019
Received in revised form 8 February 2020
Accepted 27 February 2020
Available online 28 February 2020
Handling Editor: E. Chatzi

Keywords:
Ultrasonic guided wave
Low-frequency vibration
Structural health monitoring
Aircraft primary structure
Composite materials

ABSTRACT

A reliable damage diagnostic by ultrasonic guided wave (GW) based structural health monitoring (SHM) can only be achieved if the physical interactions between wave propagation, the SHM system and environmental factors are fully understood. The purpose of this research was to gain knowledge about the effects of high-amplitude low-frequency structural vibrations (HA-LFV) and audible sound waves (SW) on ultrasonic GW propagation. Measurements were performed on a stiffened panel of a full-scale composite torsion box containing barely visible impact damage. Time-domain analysis of the filtered GW signals revealed that the main effect of HA-LFV was the presence of coherent noise. This was interpreted as the consequence of superposition of multiple dispersive wave groups produced by mode conversion at the moment of reflection on the corrugated panel surfaces during propagation. It was also observed that the coherent noise amplitude depends on the amplitude of the HA-LFV, and on the ratio between the HA-LFV frequency and the ultrasonic excitation frequency. These relationships can potentially be explored for the development of a HA-LFV compensation mechanism to enable in-service GW based damage diagnostics. In contrast, GW signals in the cases with audible SW present were almost unaffected. It was concluded that there is strong evidence supporting the hypothesis that ultrasonic GW propagation with HA-LFV effects can be analysed under the assumption of a permanently corrugated structure.
© 2020 The Authors. Published by Elsevier Ltd. This is an open access article under the CC BY-NC-ND license (http://creativecommons.org/licenses/by-nc-nd/4.0/).

1. Introduction

Ultrasonic guided waves (GWs) are recognised as one of the most promising phenomena for enabling detailed quantitative damage diagnosis in aircraft structural health monitoring (SHM) applications [1,2]. The entrance into service of GW-SHM systems is dependent on the development of capabilities to handle the uncertainty in damage diagnosis due to variable environmental-operational conditions, namely due to external dynamic mechanical perturbations on the structure. Several approaches have been studied to address time-varying boundary conditions [3–7] and loading [8,9]. However, these studies

* Corresponding author. Arubapad 8, 2315 VA, Leiden, the Netherlands.
E-mail address: p.a.viegas.ochoa.carvalho@outlook.com (P.A. Ochôa).

https://doi.org/10.1016/j.jsv.2020.115289
0022-460X/© 2020 The Authors. Published by Elsevier Ltd. This is an open access article under the CC BY-NC-ND license (http://creativecommons.org/licenses/by-nc-nd/4.0/).

do not focus on the change of the normal planar shape of the structure. GW-SHM systems are designed to operate in pre-flight and flight phases. In pre-flight preparations, the wings of an aircraft are exposed to wind gusts. During taxiing, most of the primary structure of an aircraft undergoes severe vibration. In flight, the primary structure of an aircraft is constantly subjected to vibration. All these cases constitute occurrences of high-amplitude (1–10 mm), low-frequency (relative to ultrasound) vibration (HA-LFV). Additionally, in pre-flight there are always audible sound waves (SW) coming from operating machinery (inside and outside the aircraft), and in flight most of the structure is exposed to high intensity SW produced by the engines. Therefore, if GW based SHM technology is to reach certification level, it must be able to reliably perform diagnostic with data acquired in such conditions. For that to be achieved it is first necessary to understand what are the effects of realistic audible SW and HA-LFV on ultrasonic GW propagation, and how those can be detected and compensated for.

To this date there is no known published research about the physical effects of structural vibrations on GW propagation. Still, Banerjee and Kundu [10] studied GW propagation in plates with permanent periodic shape. They developed an analytical model in order to study symmetric and anti-symmetric Lamb modes in 2D sinusoidally corrugated plates. Contrary to the wave guiding mechanism in flat plates, in which the reflected wavenumber vector always has a forward component (following Snell's law), in corrugated plates that does not always happen. In these cases, there is a resonance between the guided modes which may propagate either in opposite directions, or in the same direction. They concluded that at some frequencies, resonance between symmetric or anti-symmetric modes of different orders *"can occur when the difference between or summation of wavenumbers of the two modes is a multiple"* [10] of the plate corrugation wavenumber. At these resonances mode conversion can occur, which in turn may lead to conditions where either the wave cannot propagate, called stop bands, or multiple modes can coexist with the same phase velocity, called cross-over points.

In a more applied approach, Jiao et al. [11] investigated the use of LFV modulation of ultrasonic GW signals for the detection of nonlinear contact defects in an aluminium plate. However, the acceleration of the plate was always kept below 1 g, and the GW signals used for the defect diagnosis were synchronized with maxima and minima of the LFV cycle, which are circumstances that do not occur in real operation of structures. Recently, Radzienski et al. [12] published results of the combined use of vibration and GW testing for improved health assessment of composite panels. A sandwich panel was instrumented with a single thin piezoelectric ceramic disc which sent excitation signals formed by a continuous 2058 Hz wave periodically alternated with ultrasonic 30 kHz windowed tone-bursts. Nevertheless, it is important to note that the 2058 Hz vibration and the 30 kHz GW excitations had comparable amplitude. Additionally, when the lower frequency sine was periodically interrupted by the higher-frequency one, a synchronization pulse was sent to the acquisition unit in order to trigger the recording. These two facts prevented the overshadowing of the GW signals in the total mechanical response at the centre of the panel.

The current article presents research on reliability improvement of ultrasonic GW based SHM systems for full-scale composite aircraft primary structures. The main goal of the study was to gain knowledge about the effects of audible SW and HA-LFV on ultrasonic GW propagation. The research was based on the hypothesis that a short time window of GW propagation under audible SW or HA-LFV can be described by GW propagation in a structure with a permanently corrugated shape. The hypothesis was experimentally investigated using GW data acquired during testing of a full-scale thermoplastic composite aircraft stiffened panel subjected to representative HA-LFV and audible SW.

2. Working hypothesis

The frequency of random loads to which aircraft primary structures are typically subjected varies between 1 and 1000 Hz [13], which are frequencies 10^2 to 10^5 times lower than the typical ultrasonic GW excitation frequencies. Thus, a GW excitation pulse lasts only a short fraction of one SW/HA-LFV cycle. As a result, the SW/HA-LFV induced shape change is almost constant during the entire recorded GW time-window. Therefore, taking into account the findings by Banerjee and Kundu [10], it was established as a working hypothesis that a short time window of GW propagation under audible SW or HA-LFV can be described by GW propagation in a structure with a permanently corrugated shape. If this hypothesis is true, then the effects of audible SW and HA-LFV on GW propagation should be detectable through changes in GW arrival time and in some frequency components [10].

3. Methodology

A real-scale composite stiffened panel was excited with HA-LFV and audible SW. At the same time, ultrasonic GWs were excited and acquired at selected frequencies. To separate the damage-induced effects from the vibration-induced ones, both the damaged and non-damaged scenarios were tested. To support the conclusions drawn from the experimental analysis, and to further test the working hypothesis, finite-element (FE) modelling was employed.

For the study of the HA-LFV effects on GW propagation, it is important to highlight that the test specimen was suspended from a solid metallic frame in order to approximate free boundary conditions. The shaker was used to realistically induce high-amplitude out-of-plane displacement of the test specimen at low-frequency. Therefore, the focus was on correlating the changes in the GW signals with the vibration parameters.

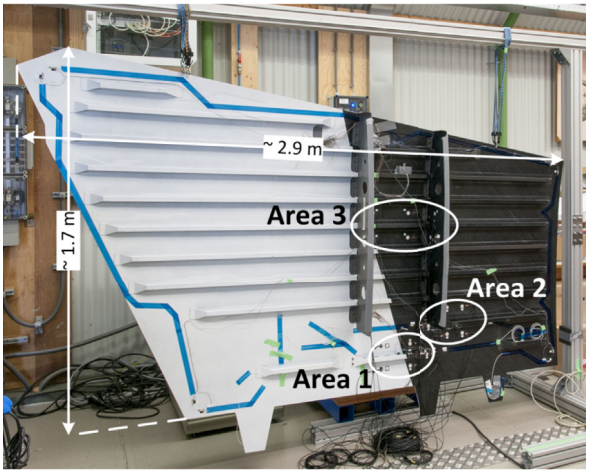

Fig. 1. General view of the torsion box panel with critical areas highlighted.

4. Experimental

The test specimen was selected as a stiffened panel of a full-scale horizontal stabilizer torsion box entirely made of carbon fibre (CF) reinforced polyetherketoneketone (PEKK), as depicted in Fig. 1. The panel was made available by Fokker Aerostructures BV for the SHM tasks of the Thermoplastic Affordable Primary Aircraft Structure 2 (TAPAS 2) project. The panel consisted of a co-consolidated stiffened skin with multiple I-stringers in butt-joint configuration, and two riveted ribs. The panel had a maximum length and width of about 2.9 and 1.7 m, respectively, with skin thickness varying between 1.8 and 8.1 mm, and rib thickness between 3 and 3.5 mm. Areas 1 and 2 (near stringer run-outs) were GW tested in pristine condition (ND) and after a 50 J impact along the stringers. The impacts were on the outer side of the skin, at the stringer run-outs of areas 1 and 2. The resulting barely visible impact damage (BVID) conditions for areas 1 and 2 are designated D1 and D2, respectively, in the analysis.

The piezoelectric ceramic (PZT) transducer network for GW measurement in areas 1 and 2 is depicted in Fig. 2. The GW testing setup can be seen in Fig. 3.

The ultrasonic excitation was produced by an Agilent 33500 B waveform generator, amplified by a TTi WA301 wideband amplifier and transmitted to the structure by thin PZT actuator discs. The ultrasonic response was sensed by thin PZT sensor discs and acquired by two digital oscilloscopes, PicoScope 4424 and PicoScope 6402 A, both connected to the same computer. All the PZT discs were made of APC 850 material (supplied by APC International, Ltd.), had a thickness of 0.4 mm and a diameter of 20 mm. Ultrasonic GWs were excited at 123, 213 and 335 kHz, using a 10-cycle sinusoidal tone-burst with the amplitude modulated by a Hanning window. The excitation signal shape and frequency, the PZT transducers geometry, and the transducer network configuration were selected according to a systematic design methodology [14] based on the optimisation of the sensor output, coupled electro-mechanical (EM) response of the transducer-structure assembly, energy transfer from the bonded PZT transducer to the structure, available area for transducer bonding, and measurement equipment capabilities. For the convenience of the reader, the design criteria are included below [14]:

A. "*The PZT sensor output function should have at least one local maximum in a frequency bandwidth where only zero-order GW modes can be excited.*"
B. "*The PZT sensor output function should have more than only one local maximum.*"

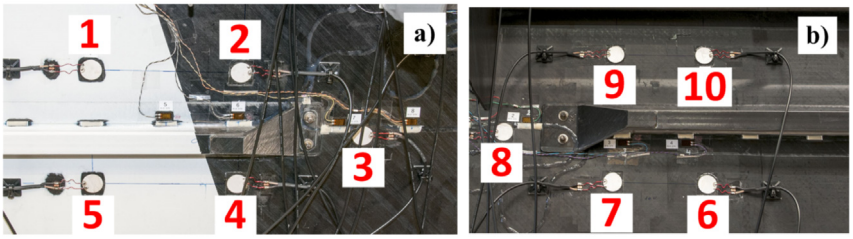

Fig. 2. Detailed view of area 1 (a) and area 2 (b) with the numbered PZT transducer locations.

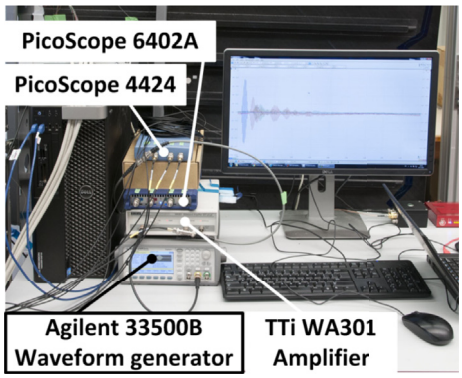

Fig. 3. Guided wave measurement setup.

C. "*The chosen frequencies should not coincide with, or be in the close vicinity of, EM resonances or anti-resonances of the bonded PZT transducer.*"
D. "*The electrical current required to drive the chosen PZT transducer at the chosen frequency should be below the maximum allowable current for the waveform generator output channels.*"
E. "*The selection of the PZT transducer thickness should take into account the maximization of the energy transfer from the actuator to the structure.*"

Additionally, a TIRAvib 50350 mechanical shaker was connected to the torsion box panel (see Fig. 4) in order to apply a single-axis, out-of-plane, HA-LFV with frequency randomly varying between 20 Hz and 1000 Hz. The amplitude randomly varied between 5 and 10 G_{RMS}, and the duration was approximately 5 min, during which GW data was also acquired. The signal of the applied HA-LFV was measured by a PCB 208A03 force transducer mounted on the connecting spigot. As shown in Fig. 5, half of the vibrational energy was concentrated at frequencies up to 100 Hz, with the rest being transmitted at more isolated components beyond 170 Hz. The sound produced by the cooling system of the shaker when in stand-by state was used to test GW propagation in the presence of audible SW. The GW signals acquired during testing were analysed in order to understand if the working hypothesis holds true. Due to constraints associated with the schedule of the test campaign, only selected "structure state + LFV" combinations were tested. During the tests with HA-LFV/SW and GWs the panel was suspended from a solid metallic frame (see Fig. 1) in order to approximate free boundary conditions.

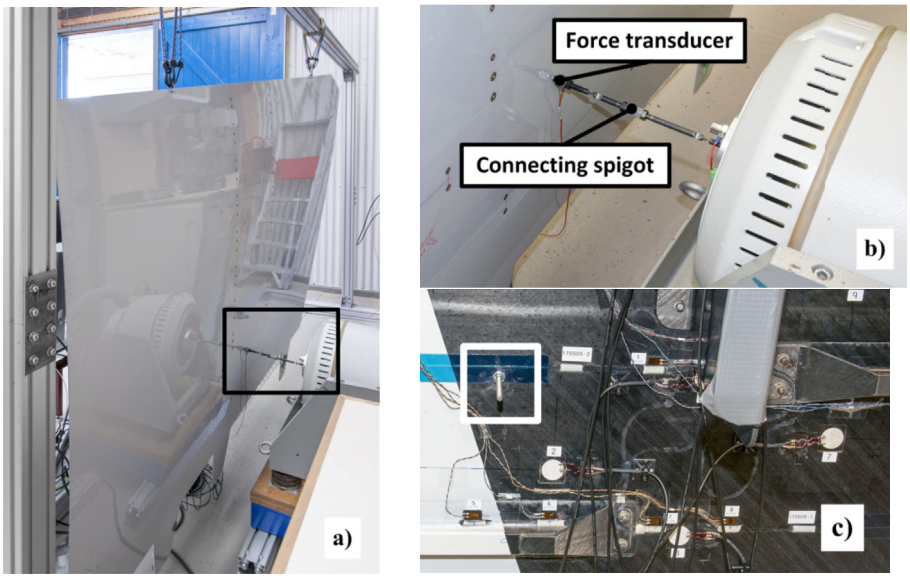

Fig. 4. Connection of the mechanical shaker to the torsion box panel: a) general view of the relative positions, b) detailed view of connecting spigot, and c) detailed view of the bolted connection on the inner side of the panel.

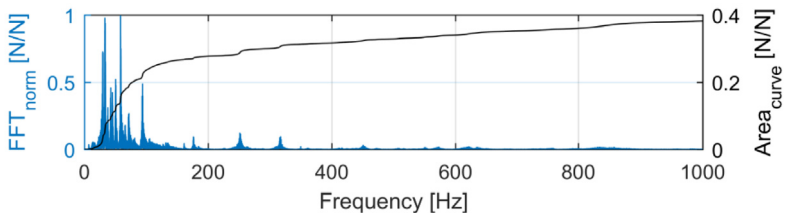

Fig. 5. Frequency spectrum of the applied HA-LFV.

5. Results and discussion

Signal plots are available as Supplementary Material in order to complete the analysis in this section. They show the raw signal, the filtered signal, and the normalised frequency spectrum in the tested cases for selected actuator-sensor pairs of areas 1 and 2. The signals for the pristine condition are also included so that the reader can compare them with the signals for the corresponding damage condition. The raw ultrasonic GW signals can also be found in [15].

5.1. High-amplitude LFV effects

5.1.1. Experimental results

As seen from Fig. 6a) the GW signal was overshadowed by HA-LFV. Therefore, continuous Morlet wavelet transform (CWT) filtering was applied to all signals in order to eliminate all the frequency components outside the -3dB band centred at the main GW excitation frequency. It is important to note that this CWT filtering was also applied to the signals acquired without the influence of HA-LFV. Thus, all signals are equally affected by the same filter-induced attenuation.

When comparing filtered signals for the cases of GW propagation without (Fig. 6b) and with (Fig. 6c) HA-LFV, background wave groups (BWGs) can be seen in the latter. If BWGs appear in the filtered signal, it means they occupy the same frequency band as the main GW signal, which indicates that they correspond to ultrasonic GWs propagating in the structure. Thus, the BWGs cannot be attributed to electrical noise from the shaker circuitry occurring at the power-line frequency or at lower integer multiples. They also cannot be attributed to fretting between the connecting spigot and the panel occurring at the HA-LFV frequency.

The observed BWGs constitute a case of coherent noise, which can be demonstrated by computing the average signal over successive acquisitions. Fig. 7 shows the band-pass filtered signals acquired by transducers 7, 8 and 9 after excitation by transducer 6 at 123 kHz in the D2 damage scenario, averaged over eight successive acquisitions. As it can be seen, the BWGs do not average out over successive acquisitions, thereby demonstrating that they correspond to coherent noise.

To provide a more tangible demonstration, it is possible to quantify the coherent noise by calculating a signal-to-background ratio (SBR) as defined in [16].

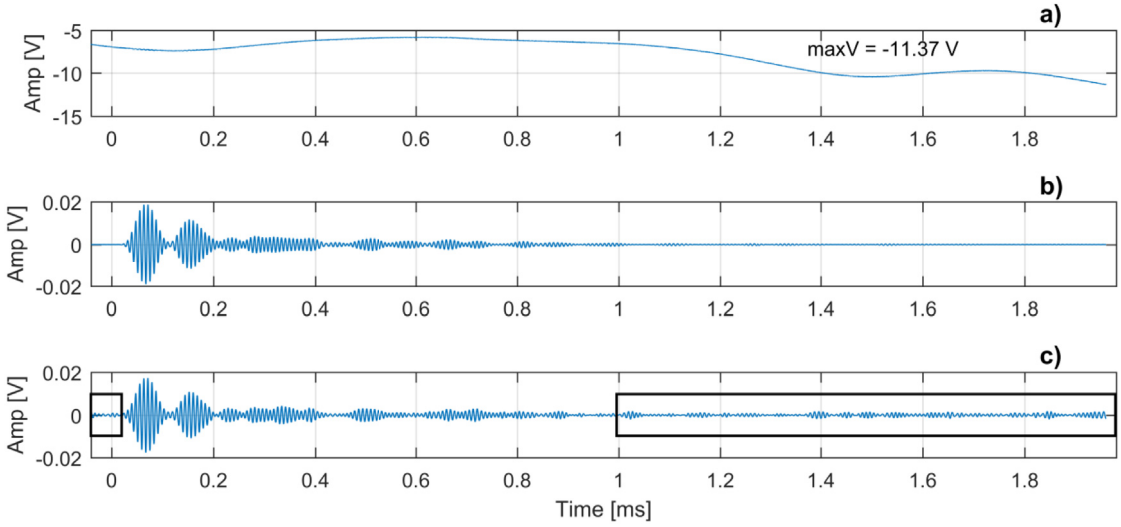

Fig. 6. Signals from actuator-sensor pair 6–9 (area 2) at 123 kHz, after 50 J impact on stringer run-out: a) raw signal with HA-LFV, b) filtered signal without HA-LFV, and c) filtered signal with HA-LFV. The background wave groups are highlighted by rectangles.

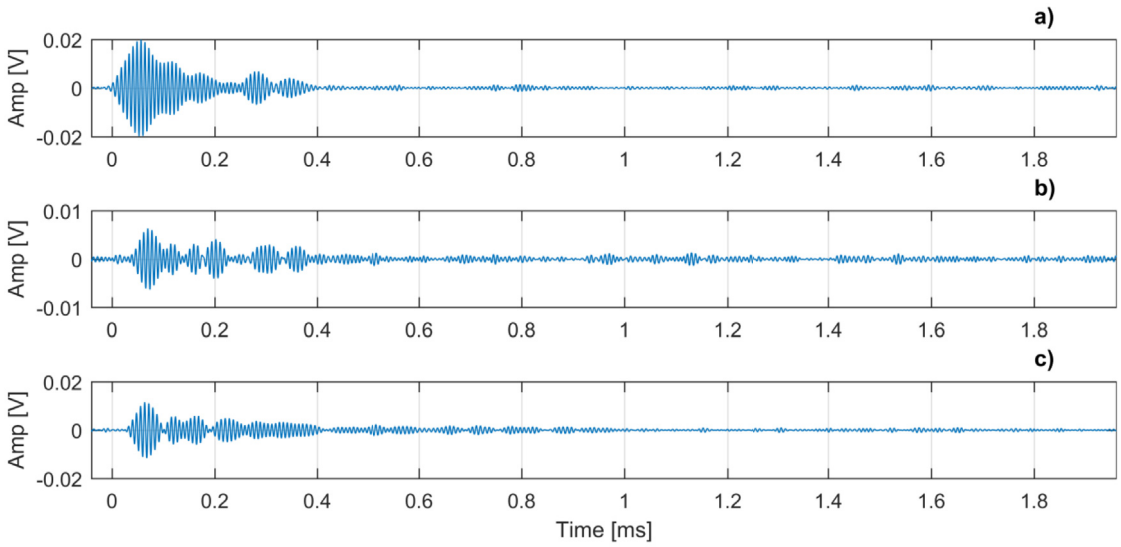

Fig. 7. Average filtered signal from actuator-sensor pair 6–7 (a), 6–8 (b) and 6–9 (c) at 123 kHz, after the 50 J impact on the stringer run-out, averaged over eight successive acquisitions.

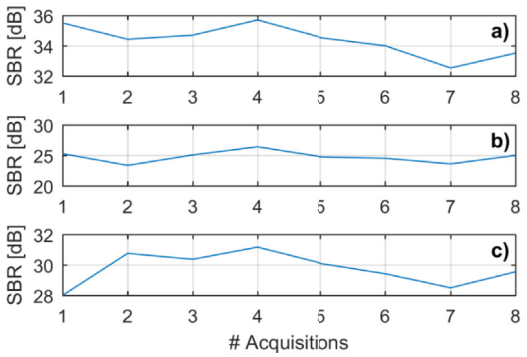

Fig. 8. Evolution of the signal-to-background ratio (SBR) with the number of acquisitions used for averaging the filtered signal from actuator-sensor pair 6–7 (a), 6–8 (b) and 6–9 (c) at 123 kHz, after the 50 J impact on the stringer run-out.

$$SBR = \left(A_{signal} \Big/ A_{back}\right)^2 = \left(Amp_{\max} / RMS_{last-third}\right)^2 \tag{1}$$

where A_{signal} is taken as the maximum amplitude of the signal, and A_{back} is taken as the root mean square (RMS) value of the last third portion of the signal. The last third portion of the signal is used for the estimate of A_{back}, because it is an interval in which there is most certainly only BWGs. In Fig. 8 the SBR is plotted as a function of the number of acquisitions used for the averaging of the signals in Fig. 7, showing that the BWG intensity remains approximately the same.

The appearance of coherent noise is interpreted as a consequence of the panel corrugated shape induced by vibration. When GWs propagate in the corrugated state of the panel the guiding mechanism takes place with more reflections at the plate surfaces per unit distance than in the non-corrugated state. Each of those reflections is accompanied by mode conversion, resulting in the generation of a higher number of dispersive wave groups per unit distance than in the non-corrugated case. The additional dispersive wave groups spread in space and time when propagating, and hence decay in amplitude, thereby overlapping and promoting the generation of coherent noise. This explanation is in line with mechanism described by Banerjee and Kundu [10]. It is also in agreement with the observations of Pedram et al. [16] who investigated the scenario of long-range ultrasonic testing, where propagation distances of 5 m or more induce a guiding mechanism with a higher number of reflections (and thus of mode conversions), thereby generating a higher number of dispersive wave groups which overlap and result in coherent noise.

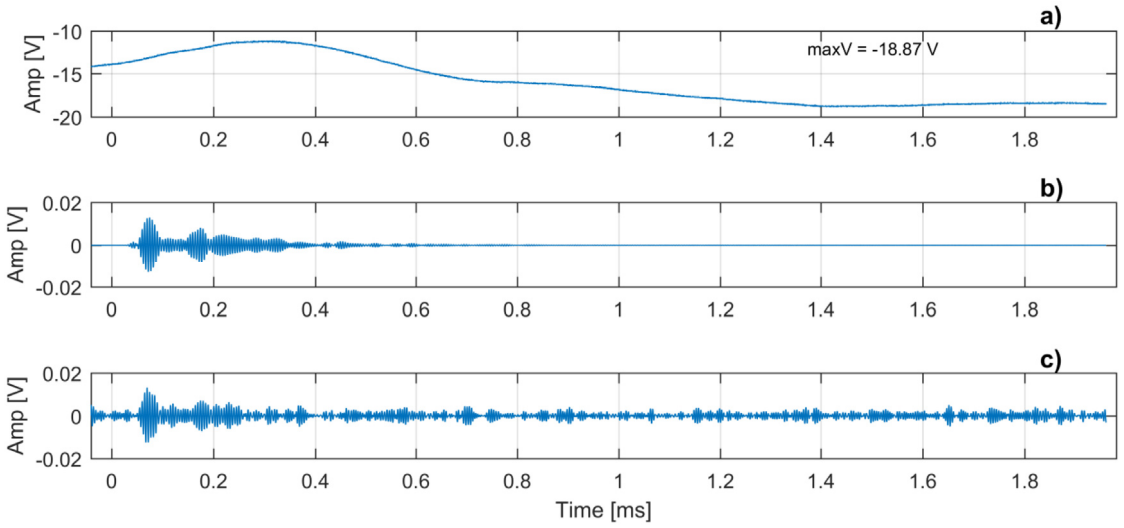

Fig. 9. Signals from actuator-sensor pair 6–9 (area 2) at 213 kHz, after 50 J impact on stringer run-out: a) raw signal with HA-LFV, b) filtered signal without HA-LFV, and c) filtered signal with HA-LFV.

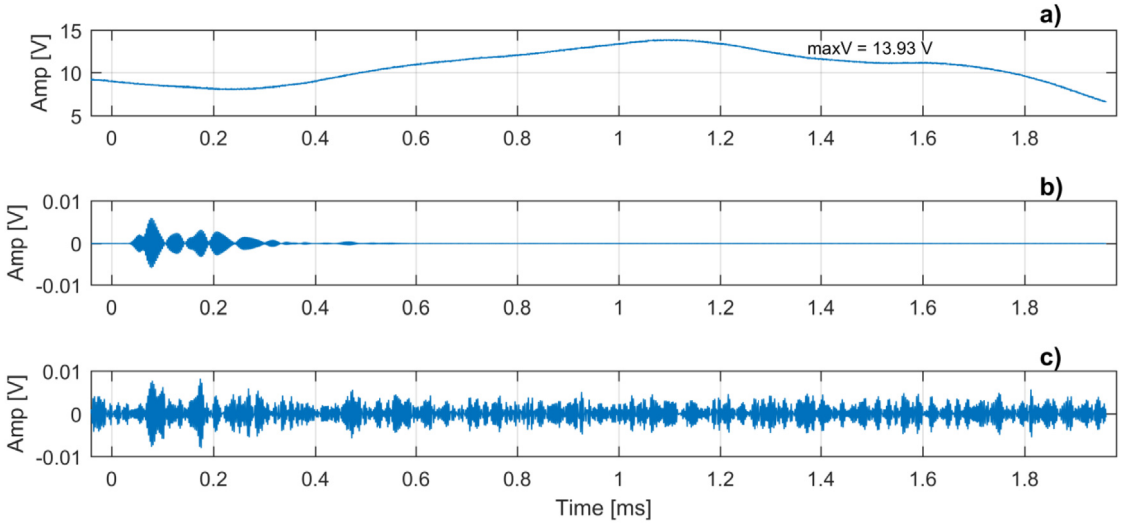

Fig. 10. Signals from actuator-sensor 6–9 (area 2) at 335 kHz, after 50 J impact on stringer run-out: a) raw signal with HA-LFV, b) filtered signal without HA-LFV, and c) filtered signal with HA-LFV.

As it can be seen from Fig. 6b), in the case without HA-LFV, the employed excitation pulse period (10 ms) allowed the acquisition of GW signals without wave groups before the main arrival. However, in the case with HA-LFV, using the same excitation pulse period, there was coherent noise before the main arrival, as shown in Fig. 6c). According to our explanation for the coherent noise, this corresponds to the lingering BWGs from the trailing edge of the previous GW signal window. This observation gives extra support to the explanation for the appearance of BWGs in the case of HA-LFV.

While in Fig. 6 and other cases the coherent noise level is relatively low, there are others where the signal of interest is partially (see Fig. 9b and c) or completely (see Fig. 10b and c) overshadowed by it.

The SBR estimates were computed for all cases (including those without HA-LFV), and the values for all tested actuator-sensor pairs in each area are plotted in Fig. 11. The SBR decreased for all cases tested under HA-LFV, meaning that coherent noise was always induced by the HA-LFV. It is interesting to note that all actuator-sensor pairs for the cases D1+LFV at 123 kHz and D2+LFV at 123 kHz were less strongly affected than for all the other cases, with SBR reductions between −9 and −16.5 dB with respect to the non-HA-LFV counterparts.

It seems thus that the intensity of the coherent noise depends not only on the amplitude of the HA-LFV (which controls the height of the plate corrugation), but also on the ratio between the ultrasonic excitation frequency (which determines the

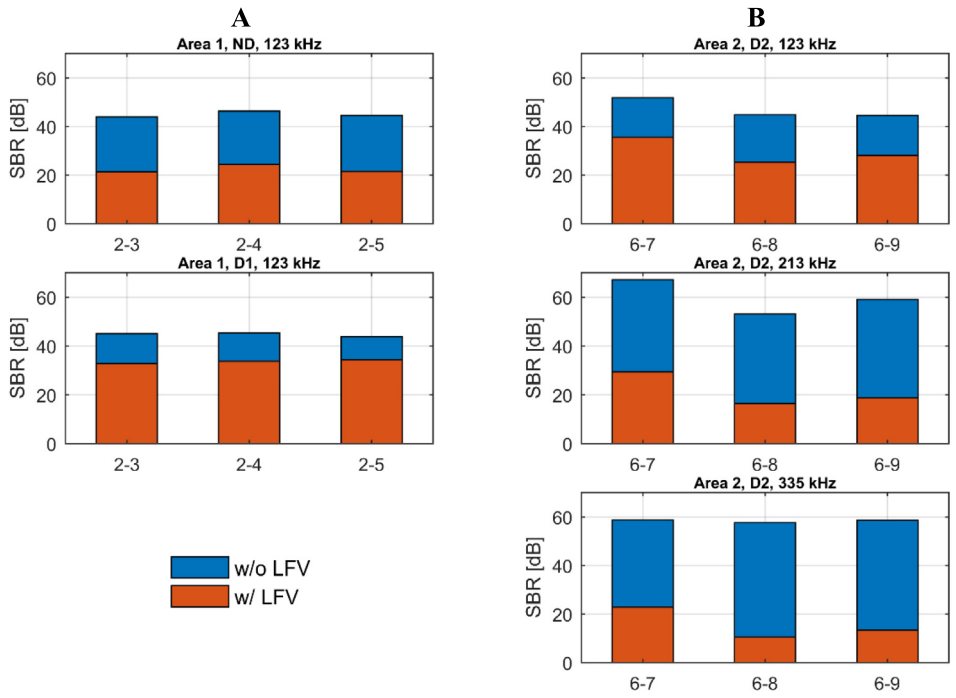

Fig. 11. Signal-to-background ratio (SBR) in the cases with HA-LFV for all tested actuator-sensor pairs of area 1 (column A) and area 2 (column B). Actuator-sensor pairs are indicated in the horizontal axis.

dispersive properties of the propagating GW modes) and the HA-LFV frequency (which determines the vibration mode shape of the panel and the corrugation wavenumber, and hence the number of reflections per unit distance). For example, in Figs. 6 and 10 the raw signals have similar LFV amplitudes (between 11 and 14 V) but in the second one the filtered GW signal is completely overshadowed by the coherent noise, which seems to be related to the aforementioned frequency ratio.

To analyse the cases at 335 kHz it is helpful to look at the theoretical group velocity dispersion curves depicted in Fig. 12, which were computed with DISPERSE® by using the composite elastic properties in Table 1, and the symmetric and quasi-isotropic stacking sequence in Table 2.

At 335 kHz there are six ultrasonic GW modes propagating in a highly dispersive regime, dividing the energy among them, and thereby attenuating much faster with propagation distance than at 123 or 213 kHz. As a result, for the cases without HA-LFV, the GW signals acquired at 335 kHz have lower amplitude than at 123 or 213 kHz, as shown in Fig. 13. In the presence of HA-LFV, the extra BWGs end up having the same amplitude as the wave packets of interest, preventing an unambiguous assessment. The influence of ultrasonic excitation frequency on the SBR is clear in the trend observed for area 2 (column B of Fig. 11).

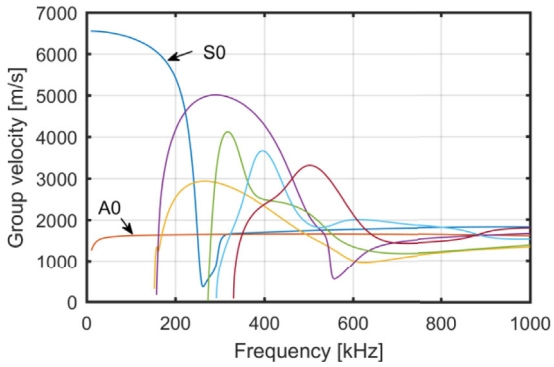

Fig. 12. Group velocity dispersion curves for the skin of areas 1–2. For clarity purposes, higher-order modes with cut-off frequencies above 400 kHz (i.e. modes that were not excited in any of the tests) are not presented.

Table 1
Elastic properties of the CF/PEKK composite material used of for the torsion-box panel, as provided by Fokker Aerostructures BV.

E_{11} [MPa]	E_{22} [MPa]	E_{33} [MPa]	G_{12} [MPa]	G_{13} [MPa]	G_{23} [MPa]	ν_{12}	ν_{13}	ν_{23}	ρ [kg/m^3]
141000	10400	10400	5460	5460	3320	0.3	0.3	0.45	1560

Table 2
Approximate stacking sequence of the composite plies for the panel skin of areas 1 and 2.

	Stacking sequence
Ply fibre orientation [°]	$[135/45/0/90]_S$
Ply thickness [mm]	$[0.53/0.53/0.80/0.65]_S$

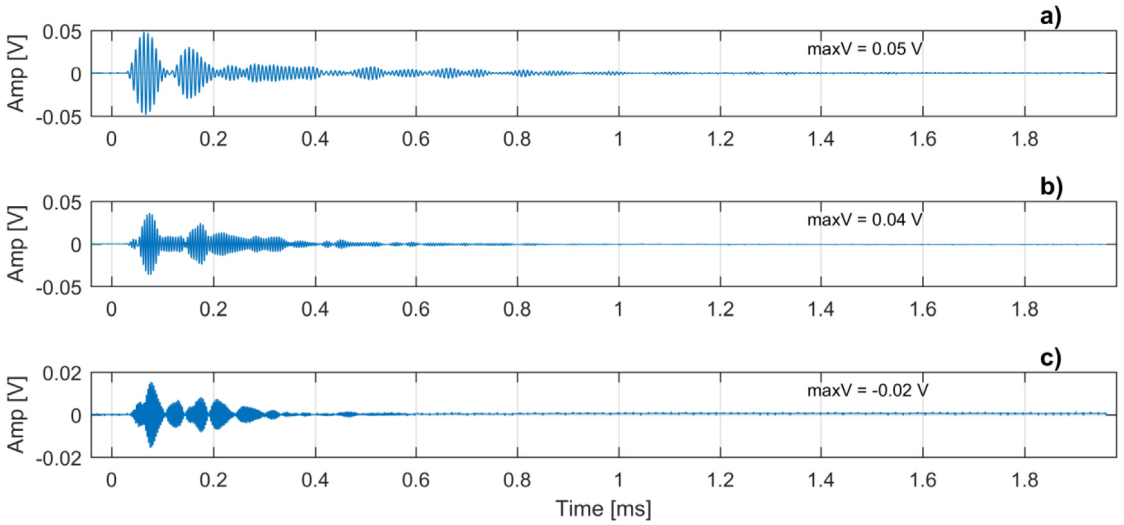

Fig. 13. Raw signals from actuator-sensor pair 6–9 (area 2), without HA-LFV, after 50 J impact on stringer run-out: at a) 123 kHz, b) 213 kHz, and c) 335 kHz.

The effect of HA-LFV on GW signals can be further quantified by time- and frequency-domain metrics, which can provide extra information about the physical interaction between the two phenomena and thereby help in testing the working hypothesis. Two quantities were selected for analysis. One was the 10%-duration time, $t_{10\%}$ [17], which is defined as the time it takes for the signal amplitude to decay from its maximum to 10% of its value. The relative variation of $\Delta t_{10\%}$ between the reference (subscript *ref*) and the new (subscript *new*) states can be calculated by:

$$\Delta t_{10\%} = \frac{\left| t_{10\%,ref} - t_{10\%,new} \right|}{t_{10\%,ref}} \tag{2}$$

The other quantity was the characteristic frequency, f_{ch}, which can be calculated as the average of all f_i frequencies in the FFT signal, weighted by the corresponding FFT coefficients [18]:

$$f_{ch} = \frac{\sum_{i=1}^{N} FFT_i \cdot f_i}{\sum_{i=1}^{N} FFT_i} \tag{3}$$

The relative variation of f_{ch} can be defined as:

$$\Delta f_{ch} = \frac{\left| f_{ch,\,ref} - f_{ch,\,new} \right|}{f_{ch,\,ref}} \tag{4}$$

Considering first the changes induced by the small BVID of D1 and D2 plotted in Fig. 14, $t_{10\%}$ shows no variation for some propagation paths, while for other propagation paths it varies approximately between 3% and 7%. The Δf_{ch} remains always between 0% and 0.7%. Hence, $\Delta t_{10\%}$ reveals the changes in the GW scattered field induced by the presence of the BVID. As a result of GWs scattering at the BVID, a higher number of wave groups are generated along the propagation path than in the ND condition. In turn, these extra wave groups interfere with the directly arriving ones, thereby inducing phase changes with respect to the baseline.

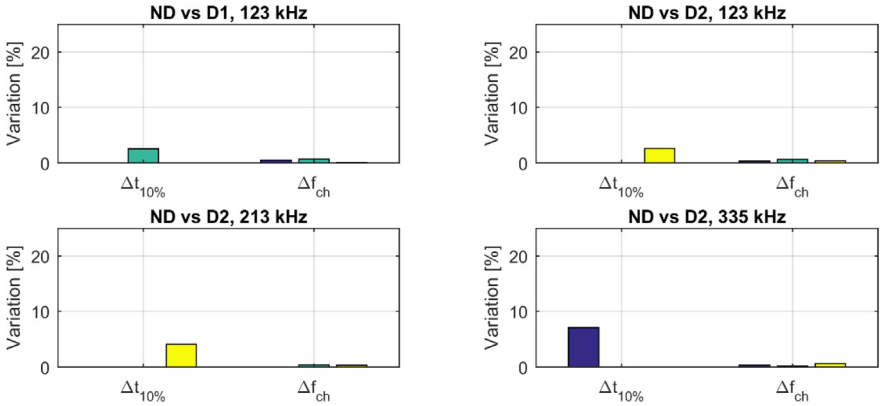

Fig. 14. Variation of 10%-duration time ($t_{10\%}$) and characteristic frequency (f_{ch}) due to differences in GW scattering at the damage, for the tested actuator-sensor pairs in areas 1 (ND vs D1) and 2 (ND vs D2), for the different excitation frequencies. The three bars (purple, green, yellow) for each quantity correspond to the three actuator-sensor pairs analysed in each area: 2–3, 2–4 and 2–5 in area 1; 6–7, 6–8 and 6–9 in area 2. (For interpretation of the references to colour in this figure legend, the reader is referred to the Web version of this article.)

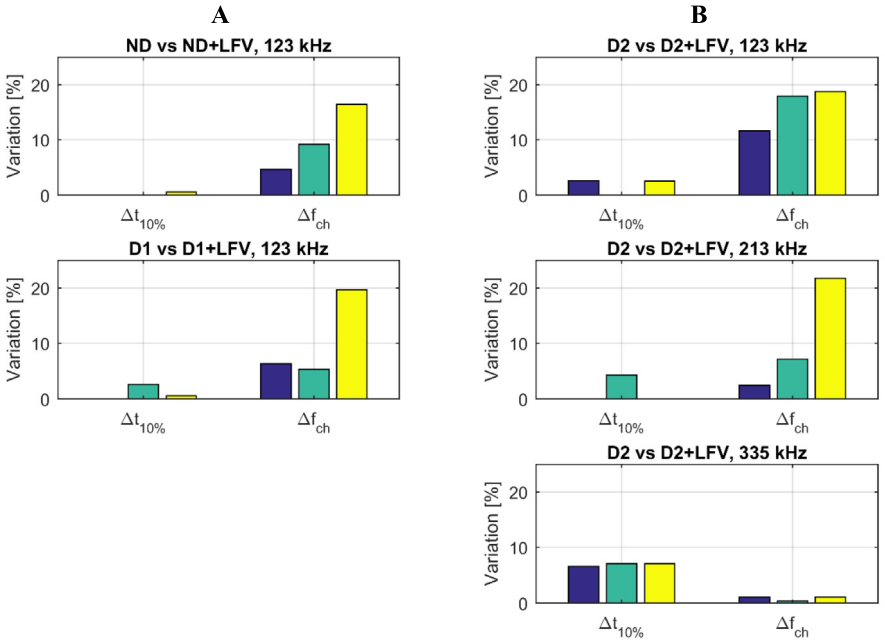

Fig. 15. Variation of 10%-duration time ($t_{10\%}$) and characteristic frequency (f_{ch}) due to the HA-LFV for all tested actuator-sensor pairs of area 1 (column A) and area 2 (column B). The three bars (purple, green, yellow) for each quantity correspond to the three actuator-sensor pair analysed in each area: 2–3, 2–4 and 2–5 in area 1; 6–7, 6–8 and 6–9 in area 2. (For interpretation of the references to colour in this figure legend, the reader is referred to the Web version of this article.)

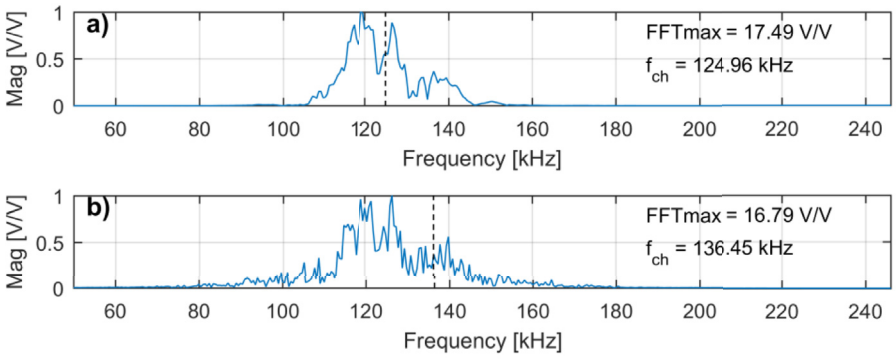

Fig. 16. Normalised FFT spectra of the signals from actuator-sensor pair 2–4 (area 1) at 123 kHz, for the ND scenario a) without HA-LFV, and b) with HA-LFV.

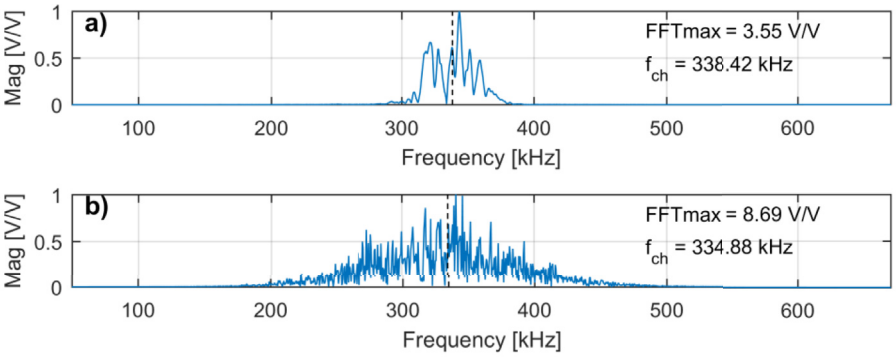

Fig. 17. Normalised FFT spectra of the signals from actuator-sensor pair 6–9 (area 2) at 335 kHz, for the D2 scenario a) without HA-LFV, and b) with HA-LFV.

Looking now at the cases with HA-LFV in Fig. 15, $t_{10\%}$ varies mostly between 2.6% and 7.1%, with some propagation paths not revealing any change. So, $\Delta t_{10\%}$ has values similar to those caused by the occurrence of D1 and D2. Thus, the phase changes caused by the BWGs seem to be equivalent to the phase changes caused by the extra wave groups generated after scattering at the BVID. It is relevant to note that the case of D2+LFV at 335 kHz had the highest $\Delta t_{10\%}$ and the highest ΔSBR in Fig. 11.

For the majority of the cases, f_{ch} shows variations between 5% and 20%. The effects on the characteristic frequency can be clearly visualized through the comparison of FFT spectra in Fig. 16. In comparison to the cases without HA-LFV (e.g. Fig. 16a), the filtered signals acquired under HA-LFV (e.g. Fig. 16b) have multiple, small frequency components spread along the sides of the useful bandwidth, which are the result of the interference between BWGs.

For the case of D2+LFV at 335 kHz (bottom graph in column B of Fig. 15), Δf_{ch} remains between 0.4% and 1.1%, which seems to be an exception to the trend observed at the other frequencies. However, this has to do with the low amplitude of the wave packets of interest at this frequency. At 335 kHz, the BWGs amplitude is comparable or equal to the amplitude of the wave packets of interest (as shown in Fig. 10), resulting in an FFT spectrum where the magnitude of the frequency components corresponding to the wave packets of interest are not prominent (see Fig. 17). In other words, the FFT spectrum is much flatter than at 123 or 213 kHz. Therefore, the weighting of the average of the FFT coefficients is balanced out, preventing the f_{ch} shift from being clearly revealed. Hence, if the maximum amplitude of the GW signal acquired without HA-LFV was higher than 0.01 V, Δf_{ch} would be expected to follow the trend observed at the other frequencies.

5.1.2. Numerical results

In an effort to further investigate the dependency of the coherent noise on the HA-LFV amplitude and on the LFV-GW frequency ratio, and to further test the working hypothesis, it was decided to build a fully three-dimensional (3D) model of a square aluminium plate with a permanently corrugated shape, with two thin PZT discs for GW actuation and sensing, as represented in Fig. 18.

Wave-based methods [19] have been developed as a way of improving the efficiency of numerical ultrasonic simulations, and the most common among them is the spectral finite element (SFE) method [20], also called the semi-analytical finite element (SAFE) method [21,22]. However, the finite-element (FE) method is still the one providing high accuracy in simulating 3D wave interactions at different space-time scales [23–25] and extensive, readily available modelling tools. Therefore, the commercial programme Abaqus/Explicit (Dassault Systèmes) was employed to develop our FE model.

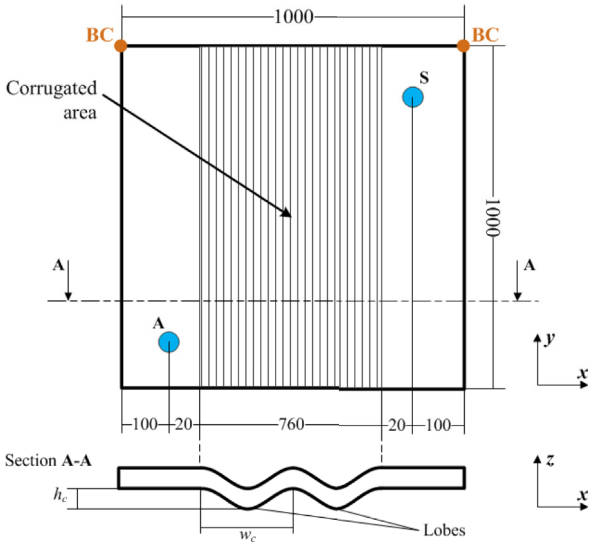

Fig. 18. Definition of the geometry of the model of the plate with permanent corrugated shape. The GW actuator and sensor are indicated with "A" and "S", respectively. The $U_x = U_y = U_z = 0$ boundary conditions are applied on the two top vertices of the upper surface indicated by the BC circles. All dimensions are in millimetres.

Boundary conditions (BC) were applied to the two top vertices of the upper surface by blocking the displacements in all directions. The dimensions of the plate were 1 m × 1 m × 2 mm, and the PZT discs had a diameter of 20 mm and a thickness of 0.4 mm. The actuator was positioned at $(x, y) = (0.1, 0.1)$ m, while the sensor was at $(x, y) = (0.9, 0.9)$ m. The permanently corrugated shape of the region between the two transducers was defined by a periodic geometry based on the corrugation height, h_c, and the corrugation wavelength, $w_c = 760/\#\text{Lobes}$, as illustrated in Fig. 18.

All the regions were defined as deformable three-dimensional volumes. The actuator/sensor adhesive layer was assumed to be infinitesimally thin, and the connection between the plate region and the actuator/sensor patch region was ensured by a tie constraint. The ultrasonic excitation was introduced by applying distributed perpendicular forces (i.e. pressure) on the circular and cylindrical faces of the actuator patch.

Table 3
Properties of the APC 850 piezoelectric ceramic material [35,36]. The compliances (indicated with '*') were obtained by inversion of the elastic stiffness matrix.

Property	Value ($\times 10^{10}$)	Property	Value ($\times 10^{-12}$)	Property	Value
c_{11}^E [N/m^2]	13.14	s_{11}^E [m^2/N]	15.70 '*'	ρ [kg/m^3]	7600
c_{12}^E [N/m^2]	8.23	s_{12}^E [m^2/N]	−4.67 '*'	ν [−]	0.35
c_{13}^E [N/m^2]	8.68	e_{31} [N/Vm]	6.91		
c_{33}^E [N/m^2]	12.25	e_{33} [N/Vm]	16.41		
c_{44}^E [N/m^2]	1.92	e_{15} [N/Vm]	13.65		

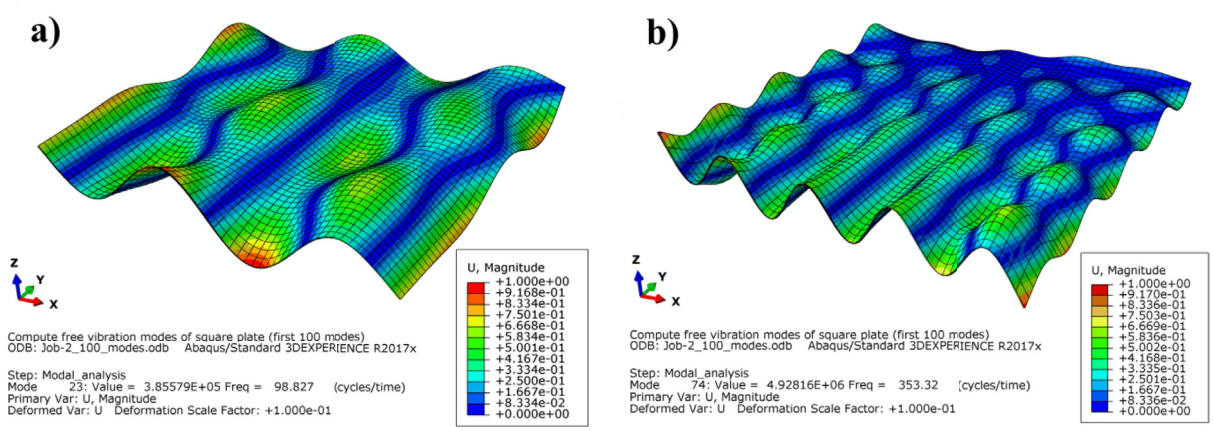

Fig. 19. Free vibration mode shape 23 at around 100 Hz (a) and 74 at around 353 Hz (b) for the modelled aluminium plate.

Table 4
Runs of the FE parametric study.

Run	GW freq [kHz]	# Lobes]	w_c [mm]	h_c [mm]
1	50	0	0	0
2		2	380	15
3				30
4		5	152	15
5				30
6	100	0	0	0
7		2	380	15
8				30
9		5	152	15
10				30
11	200	0	0	0
12		2	380	15
13				30
14		5	152	15
15				30
16	300	0	0	0
17		2	380	15
18				30
19		5	152	15
20				30

The structured mesh was formed by solid, 3D, 8-node, linear, reduced-integration elements (C3D8R) [19–30]. For correct spatial representation of the GW propagation, twenty elements per wavelength of S0 Lamb wave mode were defined along the in-plane propagation directions. Eight elements were defined along the thickness of the plate [27,29,31,32] and one element along the thickness of the PZT patches.

To ensure that the time-step was always shorter than the time required for the fastest wave component to propagate to an adjacent element (as stipulated by the Courant-Friedrichs-Lewy condition [33]), i.e. to always ensure convergence of the numerical solution, the simulation time-step was automatically defined in Abaqus by checking the stability condition element by element.

The aluminium material was modelled as isotropic homogeneous, with a Young's modulus of 70 GPa, a density of 2700 kg/m^3 and a Poisson's ratio of 0.33 [34]. The material for the PZT actuator and sensor was modelled as orthotropic homogeneous material, with elastic properties equal to those of American Piezo, Ltd. APC 850 material [35,36], as listed in Table 3.

The adopted approach for simulating the GW excitation load was based on the *PZT force model* by Nieuwenhuis et al. [37]. If the PZT disc is assumed to be in free space (i.e. not bonded to any structure), then the stresses on the disc are null and the strain generated in the material by an applied electric field would be equivalent to having external stresses acting on the disc. The stress generated in the bonded PZT by an applied electric field can be approximated by those same external forces. Hence, the ultrasonic excitation was introduced by applying distributed perpendicular forces (i.e. pressure) on the faces of the actuator disc. The value of those stresses was computed based on the piezoelectric constitutive equations [35] for an excitation tone-burst maximum amplitude of 16 V. The GW excitation was a 5-cycle tone-burst with amplitude modulated by a Hanning window. The ultrasonic GW response was taken from the out-of-plane displacement of the centre node of the top surface of the sensor disc.

To ensure the plate corrugated shape was modelled in a realistic way, Abaqus/Standard was used to perform a modal analysis to obtain the first hundred free vibration mode shapes. In this case, the structured mesh was formed by solid, 3D, 20-node, quadratic, reduced-integration elements (C3D20R) to allow enough spatial resolution with fifty elements along the plate side. Following the frequency components observed in the HA-LFV spectrum in Fig. 5a), mode 23 (at around 100 Hz) and mode 74 (at around 353 Hz) were selected, as depicted in Fig. 19. These were then the basis for defining the number of corrugation lobes and parameter w_c: 2 lobes for 100 Hz, 5 lobes for 353 Hz. The parameter h_c was defined based on the vibration amplitude estimates made during the tests of the torsion-box panel.

A parametric study was conducted by varying the GW excitation frequency, the number of corrugation lobes and the corrugation height. The executed runs are summarised in Table 4, and the numerical signals are available in Ref. [38].

Since it was decided not to implement any absorption layer, the numerical signals contain the reflections from the plate edges. Therefore, the analysis was focused on the directly arriving wave groups. The simulated time windows were as follows: [0; 0.86] ms for 50 kHz, [0; 0.6] ms for 100 kHz, [0; 0.55] ms for 200 kHz, and [0; 0.5] ms for 300 kHz.

Fig. 20 shows the time-domain numerical signals for runs 6 to 10 up to 0.6 ms. The signals are dominated by the GW modes with a predominance of out-of-plane particle motion. Taking the theoretical group velocity dispersion curves for the 2 mm aluminium plate (see Fig. 21), at 100 kHz, the first S0 mode arrives slightly after 0.2 ms and the first A0 mode slightly after

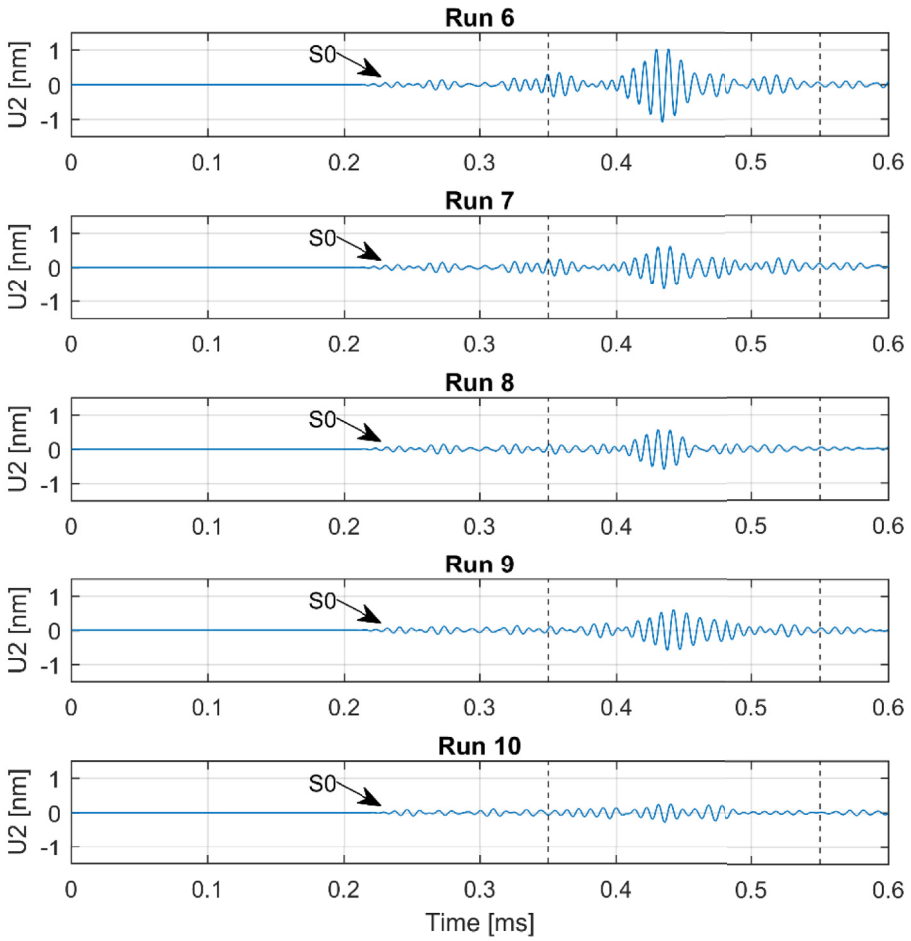

Fig. 20. Numerical time-domain signals for runs 6 to 10. The dashed lines delimit the window used for the analysis.

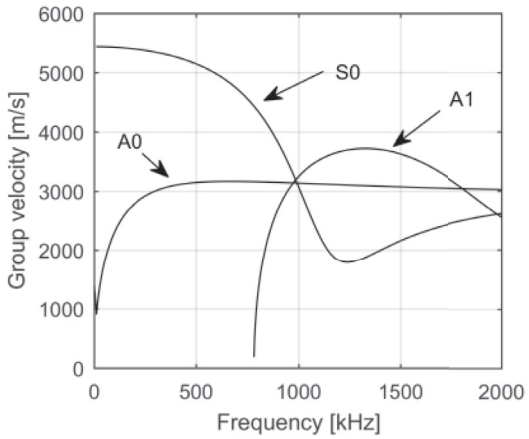

Fig. 21. Group velocity dispersion curves for the aluminium plate with 2 mm thickness (computed with DISPERSE®).

0.4 ms. Hence, the following analysis focuses on the signal window between 0.35 and 0.55 ms, delimited by the dashed lines in Fig. 20.

While the directly arriving S0 mode remains the same from run 6 to 10, the directly arriving A0 mode loses amplitude and spreads when the panel surface is corrugated. Both the amplitude loss and the spreading increase with increasing corrugation

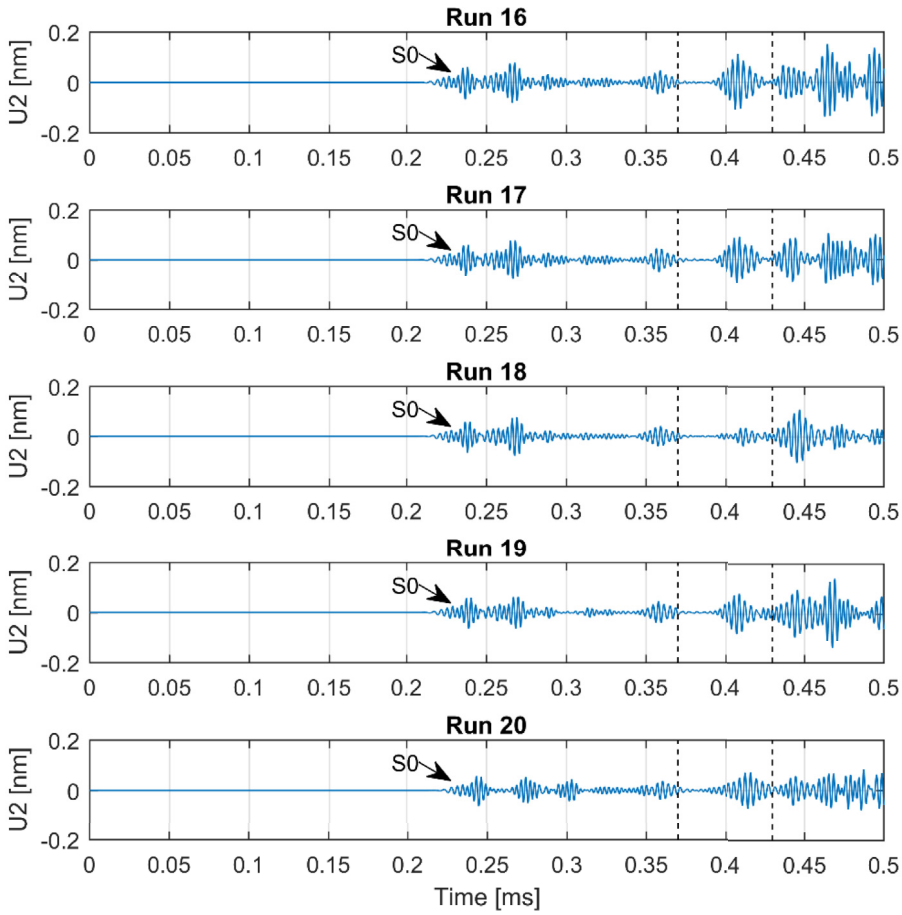

Fig. 22. Numerical time-domain signals for runs 16 to 20. The dashed lines delimit the window used for the analysis.

height and with increasing number of corrugation lobes, with the most severe case being run 10. The changes observed in the numerical signals can be explained by following the rationale put forward in Section 5.1.1 to explain the coherent noise in the experimental signals. The corrugated shape of the plate induces more reflections and mode conversions along the propagation path, and hence the generation of a larger number of dispersive wave groups which destructively interfere with the directly arriving A0 mode.

The exact same tendency can be observed in Fig. 22 for runs 16 to 20 by looking at the window between 0.37 and 0.43 ms (at 300 kHz, the first S0 mode also arrives slightly after 0.2 ms and the first A0 mode slightly before 0.4 ms).

In the frequency domain, one can, for example, observe the spectrum for runs 11 to 15 plotted in Fig. 23. Just like in Fig. 16 at the end of Section 5.1.1, the multiple frequency components along the sides of the useful bandwidth gain magnitude as corrugation is introduced. The effect of corrugation height increase is visible through the increase in the number of side peaks-valleys, such as from run 11 to 12, from run 12 to 13, and from run 14 to 15. A more severe change in the frequency content of the useful bandwidth occurs from run 11 to runs 14 and 15, with some components below 150 kHz, around 175 kHz and above 200 kHz being strongly attenuated, while some between 200 and 250 kHz and beyond 250 kHz being strengthened. This seems to agree with the hypothesis that the number of interfering wave groups increases with the number of corrugation lobes, i.e. with the LFV frequency. By comparing runs 11 to 15, one may argue that while the number of corrugation lobes (i.e. HA-LFV frequency) seems to control the number of interfering wave groups, the corrugation height (i.e. HA-LFV amplitude) seems to control the constructiveness/destructiveness of the interference through phase differences after reflection.

Using Eq. (1) with A_{back} equal to the RMS value of the analysed signal window, it is possible to have a measure of the prominence of the A0 mode with respect to the wave groups in the immediate vicinity. By taking the free plate vibration frequencies associated to the corrugation lobes (100 Hz for 2 lobes, 353 Hz for 5 lobes), it is possible to plot the percent variation of SBR as a function of LFV-GW frequency ratio (F_{LFV}/F_{GW}), for different corrugation heights, as in Fig. 24. The destructive interference trend which was qualitatively explained for Figs. 20 and 22 can thus be evaluated quantitatively. It

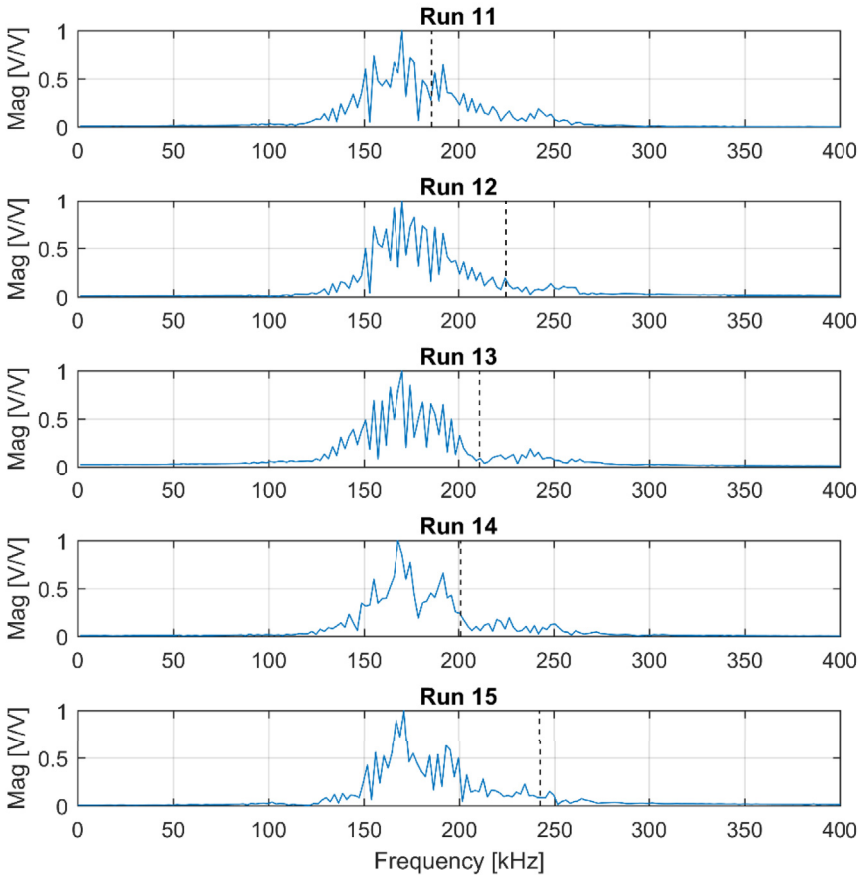

Fig. 23. Normalised FFT spectra for run 11 to 15. The dashed line indicates the characteristic frequency.

seems valid to state that corrugation height has a slightly stronger influence on the intensity of BWGs generation than F_{LFV}/F_{GW}.

Fig. 25 presents the variation of $t_{10\%}$ and f_{ch} computed for the analysed signal windows ([0.58; 0.79] ms for 50 kHz, [0.35; 0.55] ms for 100 kHz, [0.39; 0.46] ms for 200 kHz, and [0.37; 0.43] ms for 300 kHz) as function of F_{LFV}/F_{GW}, for different

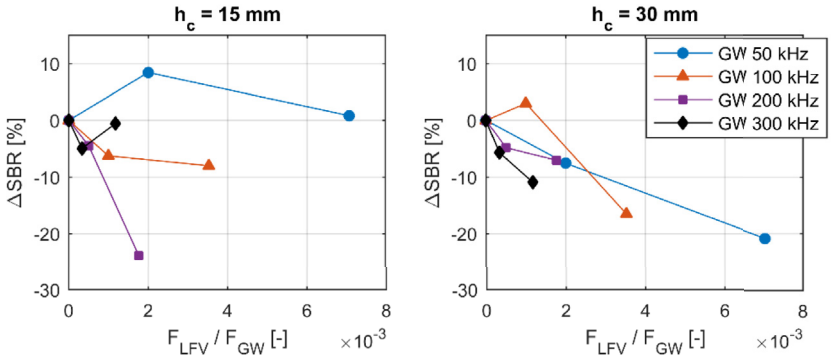

Fig. 24. Variation of signal-to-background ratio (SBR) in the numerical signals as a function of LFV-GW frequency ratio for a corrugation height of a) 15 mm and b) 30 mm.

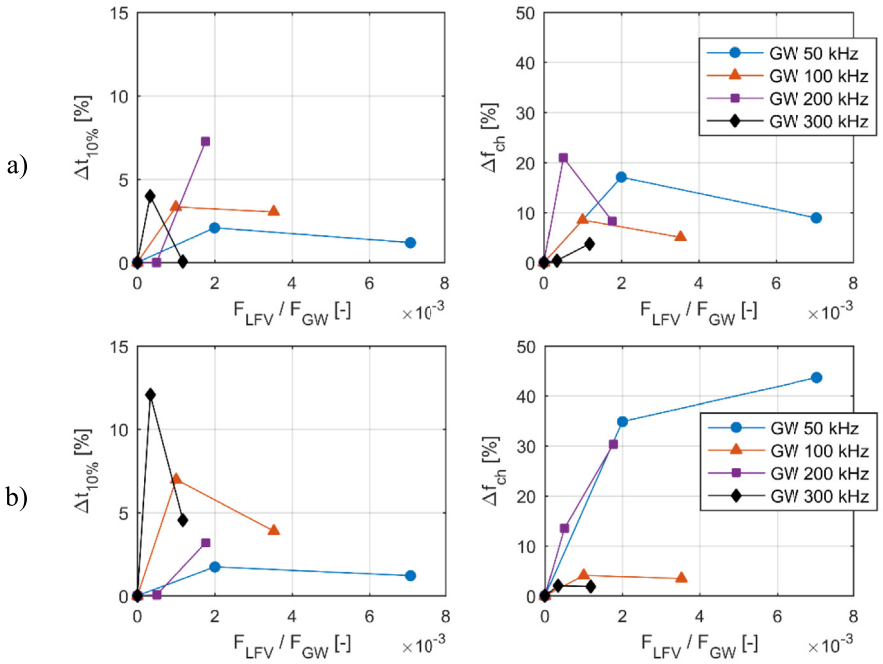

Fig. 25. Variation of 10%-duration time ($t_{10\%}$) and characteristic frequency (f_{ch}) in the numerical signals as a function of LFV-GW frequency ratio for a corrugation height of a) 15 mm and b) 30 mm.

corrugation heights. It is important to highlight that the ranges of $\Delta t_{10\%}$ and Δf_{ch} are similar to those obtained experimentally and presented in Fig. 15. The increase in $t_{10\%}$ with increasing F_{LFV}/F_{GW} is higher for a corrugation height of 30 mm than for 15 mm, which connects back to the stronger influence of corrugation height on the BWGs and their interference with directly arriving wave groups.

At this point, it seems valid to state that the conjugation of moderate changes in $t_{10\%}$ and in f_{ch} is strongly correlated with the presence of HA-LFV effects on ultrasonic GW propagation. Most importantly, there seems to be enough evidence to confirm the working hypothesis that a short time window of GW propagation under HA-LFV can be described by GW propagation in a structure with a permanently corrugated shape.

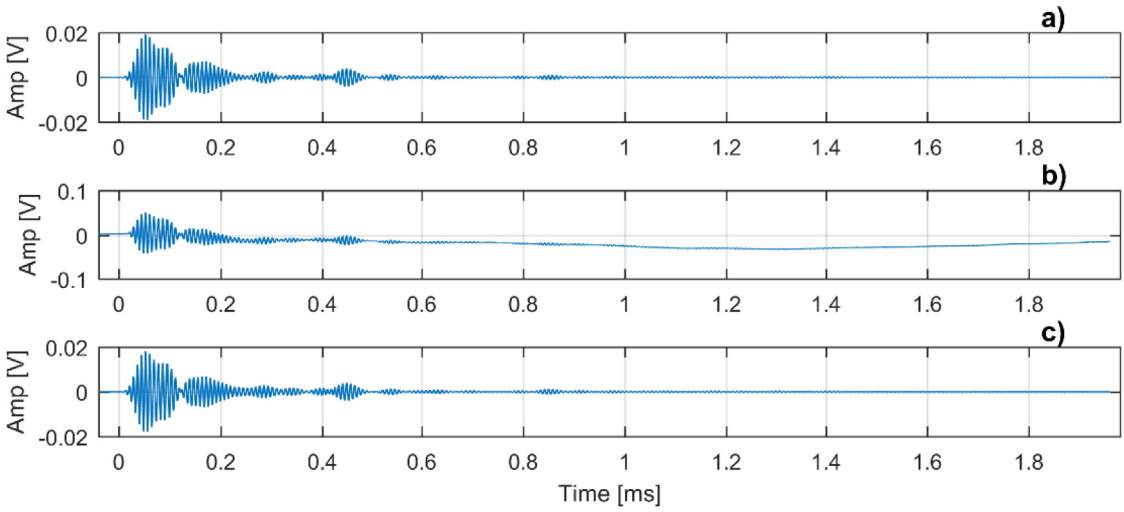

Fig. 26. Signals from actuator-sensor pair 2–4 (area 1) at 123 kHz, after 50 J impact on stringer run-out: a) filtered signal without SW, b) raw signal with SW, and c) filtered signal with SW.

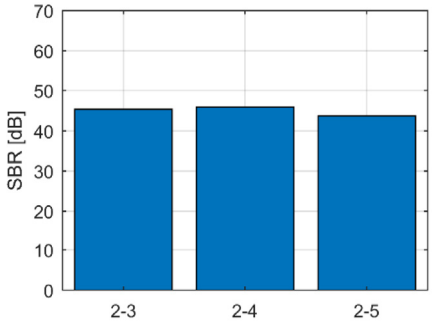

Fig. 27. Signal-to-background ratio (SBR) for all actuator-sensor pairs of area 1, after 50 J impact on stringer run-out, with audible SW.

5.2. Audible SW effects

The visual comparison of Fig. 26a) and c) shows there was no coherent noise in the filtered signals for the cases under the effect of audible SW cases, which was reflected in SBR values (Fig. 27) identical to those obtained at rest (see bar graphs for area 1, D1, 123 kHz without LFV in column A of Fig. 11). In fact, both the time-domain and the frequency-domain representations of the filtered signals look identical for all of them. As a result, the $t_{10\%}$ and f_{ch} variations (purposely omitted) were practically null. This shows that the audible SW did not induce corrugation of the panel, even though it still interacts with the PZT sensor and hence with acquired signal, as seen in Fig. 26b).

In short, when the audible SW and the GW signal have amplitudes of the same order of magnitude, there is no detectable effect in the CWT filtered signal, which in turn is in agreement with previous research [12]. However, this might not be the case if the amplitude of the SW would reach the range of 1–10 V in the raw signal. The raw signals in the HA-LFV and the SW cases have similar frequency content, as can be seen by the period of the external perturbations (see Figures SM 4 A and SM 7 A of the Supplementary Material). However, the amplitude of the external perturbations corresponding to HA-LFV was 100–1000 times higher than that corresponding to SW. Therefore, it is likely that if the SW amplitude reached values comparable to those of HA-LFV (i.e. within 1–10 V), the audible SW would have an effect on GWs.

5.3. Diagnostic capabilities under HA-LFV or SW

The relevant question at this point seems to be: *Can damage diagnosis be reliably performed in the presence of HA-LFV or audible SW?* The first thing to do before providing an answer is to look at the damage indicator (DI) values for the tested HA-LFV and SW cases and to compare them with the cases at rest. Formulations based on the CC (correlation coefficient) and the RMSD (root mean square deviation), were applied to quantify the differences in the time- and frequency-domain representations of the signals. From all of them, the frequency-domain CC-based DI (DI_{CC}) had the weakest influence of LFV/SW effects, and was thus the selected DI. The CC was computed between each normalised frequency spectrum and the corresponding baseline at rest. The obtained DI_{CC} values for the HA-LFV and audible SW cases (along with corresponding cases at rest) are plotted in Figs. 28 and 29, respectively.

From an operational point of view, the DI obtained in area 1 at 123 kHz in the ND + LFV case would lead to an erroneous diagnostic, as there was no damage present in the structure and still the DI_{CC} was around 0.1 (see first graph of Fig. 28). An erroneous diagnostic would also be obtained for area 2 in the D2+LFV cases at 213 and 335 kHz (see third and fourth graphs of Fig. 28), as no extra damage was present in the structure with respect to the D2 state and yet the DI_{CC} was increased by about 0.1 and 0.2, respectively. However, the diagnostic for area 1 at 123 kHz in the D1+LFV case (see first graph of Fig. 28), and for area 2 at 123 kHz in the D2+LFV case (see second graph of Fig. 28) would be practically the same as for the corresponding cases at rest D1 and D2, respectively.

For the audible SW cases (see Fig. 29), the DI_{CC} seems to be weakly affected for only one of the actuator-sensor pairs, which means that the diagnostic would be reliable. It is important to remember that the amplitude of the audible SW in the raw signals was of the same order of magnitude as the GW groups.

Thus, the question posed in the beginning of this section can be answered in two parts. For a system with no LFV compensation mechanism, it is possible to reliably perform diagnostic 1) only in some of the cases where HA-LFV is present; and 2) in cases where audible SW is present and has an amplitude of the same order of magnitude as the GW groups.

It is clear that a compensation mechanism would be required if damage diagnostic was required to be reliably accomplished at all times. The automated identification of LFV/SW cases is not expected to be problematic, as experience shows that raw GW signals without LFV/SW effects have amplitudes below 200 mV. Therefore, HA-LFV or audible SW cases could potentially be identified if the absolute value of the raw signal amplitude goes beyond 200–500 mV. Once that identification was done, an algorithm could use information about the relationship between amplitude and frequency of the LFV/SW and the effects on the frequency-domain representation of the filtered signal in order to define the necessary DI compensation. In

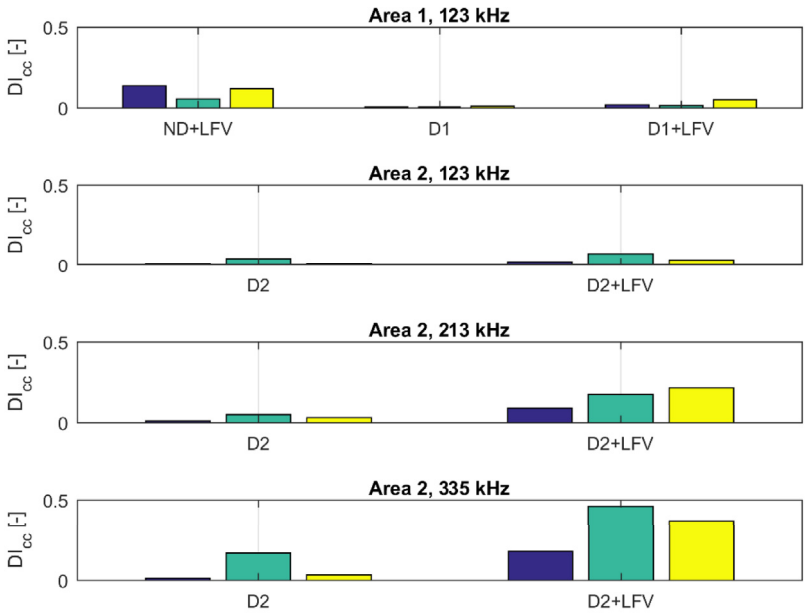

Fig. 28. Frequency-domain CC-based DI for all tested HA-LFV cases, together with corresponding reference states. The three bars (purple, green, yellow) for each condition correspond to the three actuator-sensor pair analysed in each area: 2–3, 2–4 and 2–5 in area 1; 6–7, 6–8 and 6–9 in area 2. (For interpretation of the references to colour in this figure legend, the reader is referred to the Web version of this article.)

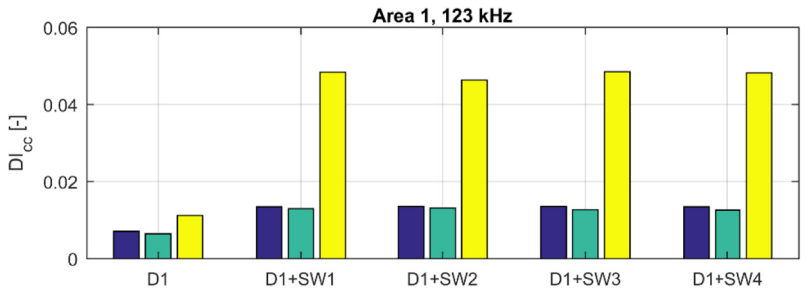

Fig. 29. Frequency-domain CC-based DI for all tested audible SW cases. The three bars (purple, green, yellow) for each condition correspond to the three actuator-sensor pairs, 2–3, 2–4 and 2–5, in area 1. (For interpretation of the references to colour in this figure legend, the reader is referred to the Web version of this article.)

this study, however, both the amplitude and frequency of the LFV were varying randomly during the tests, which prevented a relationship being established between those quantities and the observed variations of DI_{CC}, $\Delta t_{10\%}$ and Δf_{ch}. Additionally, the auxiliary FE model described in Section 5.1.2 did not include the simulation of damage, and hence did not allow the assessment of the evolution of the DI with the LFV frequency and amplitude. A potential alternative to DI compensation could be, for example, the utilization of split-spectrum signal processing [16] instead of CWT filtering in order to try to reduce the coherent noise in the GW signals.

6. Conclusions

This paper presented research on reliability improvement of ultrasonic guided wave (GW) based structural health monitoring (SHM) of full-scale composite aircraft primary structures. The main goal of the study was to gain knowledge about the effects of audible sound waves (SW) and high-amplitude low-frequency vibrations (HA-LFV) on ultrasonic GW propagation. The research was based on the hypothesis that a short time window of GW propagation under audible SW or HA-LFV can be described by GW propagation in a structure with a permanently corrugated shape.

In order to test this hypothesis, a test campaign was conducted on a stiffened panel of a full-scale horizontal stabilizer torsion box entirely made of carbon fibre reinforced thermoplastic material. Barely visible impact damage was applied to different critical locations of the structure, and GW measurements were performed before and after each state. During the

GW measurements, a mechanical shaker was used to apply a HA-LFV spectrum with randomly varying frequency and amplitude. The cooling system of the shaker in stand-by was used as source of audible SW.

The visible effect of HA-LFV on ultrasonic GW propagation was the presence of coherent noise in the filtered signals. This coherent noise was interpreted as the result of superposition of multiple dispersive wave groups produced by mode conversion at the moment of reflection on the corrugated panel surface. Strong evidence of this was found in the frequency-domain through the appearance of multiple components within the useful bandwidth, which resulted in a consistent increase of the characteristic frequency (f_{ch}). Increases in the 10%-duration time ($t_{10\%}$) of GW signals appeared to indicate phase changes, which in turn were caused by the altered scattered field in the corrugated structure. It was also observed that the coherent noise amplitude depends on the amplitude of the LFV, and on the ratio between the LFV frequency and the ultrasonic excitation frequency.

The audible SW generated by the cooling system of the mechanical shaker had a maximum amplitude of the same order of magnitude as the maximum GW amplitude. As a result, no coherent noise was observed in the filtered signals and, hence, it barely affected the diagnostic capabilities.

After using finite-element modelling to simulate GW propagation in an aluminium plate with a permanent corrugated shape, there was strong evidence supporting the hypothesis that ultrasonic GW propagation with HA-LFV effects can be analysed under the assumption of a structure with a permanent corrugated shape.

From an SHM operation point of view, reliable diagnostic was still possible in the HA-LFV cases with weaker coherent noise. The other cases would require an algorithm to be developed in order to either apply more effective filtering, or to compensate for the influence of the coherent noise on the damage indicator.

Finally, it is important to mention that to the best of the authors' knowledge the current study represents the first time research has been conducted in order to understand the effects of HA-LFV on ultrasonic GW propagation, as a means to bring GW based SHM systems closer to certification.

Funding statement

This research is part of the Thermoplastic Affordable Primary Aircraft Structure 2 (TAPAS 2) project, financed by the Netherlands Enterprise Agency of the Ministry of Economic Affairs.

Declaration of competing interests

The authors declare that they have no known competing financial interests or personal relationships that could have appeared to influence the work reported in this paper.

CRediT authorship contribution statement

Pedro A. Ochôa: Conceptualization, Methodology, Software, Formal analysis, Investigation, Data curation, Writing - original draft, Visualization. **Roger M. Groves:** Writing - review & editing, Supervision. **Rinze Benedictus:** Resources.

Acknowledgments

The authors would like to thank Frank Grooteman from the NLR-Netherlands Aerospace Centre for his collaboration before, during and after the test campaign on the torsion box panel, and Pieter Lantermans from Fokker Aerostructures B.V. for providing the torsion box panel. Last but not least, the authors would like to show their gratitude to Lourens Prikken and Dion Baptista, also from the NLR, for their support during the installation of the piezoelectric transducers on the torsion box panel.

Appendix A. Supplementary data

Supplementary data to this article can be found online at https://doi.org/10.1016/j.jsv.2020.115289.

References

[1] Z. Su, L. Ye, Y. Lu, Guided Lamb waves for identification of damage in composite structures: a review, J. Sound Vib. 295 (2006) 753–780, https://doi.org/10.1016/j.jsv.2006.01.020.
[2] M. Mitra, S. Gopalakrishnan, Guided wave based structural health monitoring: a review, Smart Mater. Struct. 25 (53001) (2016) 1–27, https://doi.org/10.1088/0964-1726/25/5/053001.
[3] I. Lopez, N. Sarigul-Klijn, A review of uncertainty in flight vehicle structural damage monitoring, diagnosis and control: challenges and opportunities, Prog. Aero. Sci. 46 (2010) 247–273, https://doi.org/10.1016/j.paerosci.2010.03.003.
[4] L.D. Avendaño-Valencia, S.D. Fassois, Gaussian mixture random coefficient model based framework for SHM in structures with time-dependent dynamics under uncertainty, Mech. Syst. Signal Process. 97 (2017) 59–83, https://doi.org/10.1016/j.ymssp.2017.04.016.
[5] L. Qiu, S. Yuan, F.K. Chang, Q. Bao, H. Mei, On-line updating Gaussian mixture model for aircraft wing spar damage evaluation under time-varying boundary condition, Smart Mater. Struct. 23 (125001) (2014) 1–14, https://doi.org/10.1088/0964-1726/23/12/125001.

[6] M. Mohabuth, A. Kotousov, C.T. Ng, L.R.F. Rose, Implication of changing loading conditions on structural health monitoring utilising guided waves, Smart Mater. Struct. 27 (25003) (2018) 1–12, https://doi.org/10.1088/1361-665X/aa9f89.
[7] Lei Qiu, F. Fang, S. Yuan, Improved density peak clustering-based adaptive Gaussian mixture model for damage monitoring in aircraft structures under time-varying conditions, Mech. Syst. Signal Process. 126 (2019) 281–304, https://doi.org/10.1016/j.ymssp.2019.01.034.
[8] N. Gandhi, J.E. Michaels, S.J. Lee, Acoustoelastic Lamb wave propagation in biaxially stressed plates, J. Acoust. Soc. Am. 132 (3) (2012) 1284–1293, https://doi.org/10.1121/1.4740491.
[9] M. Mohabuth, A. Kotousov, C.T. Ng, Effect of uniaxial stress on the propagation of higher-order Lamb wave modes, Int. J. Non Lin. Mech. 86 (2016) 104–111, https://doi.org/10.1016/j.ijnonlinmec.2016.08.006.
[10] S. Banerjee, T. Kundu, Symmetric and anti-symmetric Rayleigh-Lamb modes in sinusoidally corrugated waveguides: an analytical approach, Int. J. Solid Struct. 43 (21) (2006) 6551–6567, https://doi.org/10.1016/j.ijsolstr.2006.01.005.
[11] J.P. Jiao, B.W. Drinkwater, S.A. Neild, P.D. Wilcox, Low-frequency vibration modulation of guided waves to image nonlinear scatterers for structural health monitoring, Smart Mater. Struct. 18 (65006) (2009) 1–8, https://doi.org/10.1088/0964-1726/18/6/065006.
[12] M. Radzienski, M. Cao, X. Wei, P. Kudela, W. Ostachowicz, Combined vibration and guided wave-based approach for composite panels health assessment, Proc. SPIE 10170 (101702D) (2017) 1–8, https://doi.org/10.1117/12.2260425.
[13] J. Schijve, Fatigue of Structures and Materials, second ed., Springer, Dordrecht, Netherlands, 2009 https://doi.org/10.1007/978-1-4020-6808-9.
[14] P. Ochôa, R.M. Groves, R. Benedictus, Systematic multi-parameter design methodology for an ultrasonic health monitoring system for full-scale composite aircraft primary structures, Struct. Contr. Health Monit. (2019) e2340, https://doi.org/10.1002/stc.2340.
[15] P.A. Viegas Ochôa de Carvalho, Supporting Data for Guided Wave Tests with Structural Vibrations, 4TU.Centre for Research Data, 2019. https://doi.org/10.4121/uuid:5deaf8cf-ec57-4e33-86c4-8253a00df1d4.
[16] S.K. Pedram, S. Fateri, L. Gan, A. Haig, K. Thornicroft, Split-spectrum processing for SNR enhancement of ultrasonic guided wave, Ultrasonics 83 (2018) 48–59, https://doi.org/10.1016/j.ultras.2017.08.002.
[17] C.R. Farrar, K. Worden, Structural Health Monitoring: A Machine Learning Perspective, John Wiley & Sons, UK, 2013, https://doi.org/10.1002/9781118443118.
[18] L. Singher, Bond strength measurement by ultrasonic guided waves, Ultrasonics 35 (1997) 305–315, https://doi.org/10.1016/S0041-624X(96)00109-6.
[19] V. Thierry, L. Brown, D. Chronopoulos, Multi-scale propagation modelling for two-dimensional periodic textile composites, Compos Part B 150 (2018) 144–156, https://doi.org/10.1016/j.compositesb.2018.05.052.
[20] S. Gopalakrishnan, M. Ruzzene, S. Hanagud, Computational Techniques for Structural Health Monitoring, Springer, London, UK, 2011, https://doi.org/10.1007/978-0-85729-284-1.
[21] V. Janapati, F. Kopsaftopulos, F. Li, S.J. Lee, F.K. Chang, Damage detection sensitivity characterization of acousto-ultrasound-based SHM techniques, Struct. Health Monit. 15 (2) (2016) 143–161, https://doi.org/10.1177/1475921715627490.
[22] W. Duan, T.H. Gan, Investigation of guided wave properties of anisotropic composite laminates using a semi-analytical finite element method, Compos Part B 173 (106898) (2019) 1–10, https://doi.org/10.1016/j.compositesb.2019.106898.
[23] D. Cerniglia, A. Pantano, N. Montinaro, 3D simulations and experiments of guided wave propagation in adhesively bonded multi-layered structures, NDT&E Int 43 (2010) 527–535, https://doi.org/10.1016/j.ndteint.2010.05.009.
[24] Z. Fan, M.J.S. Lowe, Interaction of welded-guided waves with defects, NDT&E Int 47 (2012) 124–133, https://doi.org/10.1016/j.ndteint.2012.01.001.
[25] A. De Luca, F. Caputo, Z.S. Khodaei, M.H. Aliabadi, Damage characterization of composite plates under low velocity impact using ultrasonic guided waves, Composites Part B 138 (2018) 168–180, https://doi.org/10.1016/j.compositesb.2017.11.042.
[26] Abaqus 6.14 Documentation. Finite elements and rigid bodies, in: Getting Started with Abaqus, Dassault Systèmes, 2014.
[27] C.T. Ng, M. Veidt, L.R.F. Rose, C.H. Wang, Analytical and finite element prediction of Lamb wave scattering at delaminations in quasi-isotropic composite laminates, J. Sound Vib. 331 (2012) 4870–4883, https://doi.org/10.1016/j.jsv.2012.06.002.
[28] B.I.S. Murat, P. Khalili, P. Fromme, Impact damage detection in composite panels using guided ultrasonic waves, AIP Conf Proc 1581 (2014) 286–293, https://doi.org/10.1063/1.4864832.
[29] P. Manogharan, X. Yu, Z. Fan, P. Rajagopal, Interaction of shear horizontal bend (SH_B) guided mode with defects, NDT&E Int 75 (2015) 39–47, https://doi.org/10.1016/j.ndteint.2015.06.004.
[30] P. Rajagopal, M.J.S. Lowe, Scattering of the fundamental shear horizontal guided wave by a part-thickness crack in an isotropic plate, J. Acoust. Soc. Am. 124 (6) (2008) 2895–2904, https://doi.org/10.1121/1.2982410.
[31] A. Demma, P. Cawley, M. Lowe, Scattering of the fundamental shear horizontal mode from steps and notches in plates, J. Acoust. Soc. Am. 113 (4) (2003) 1880–1891, https://doi.org/10.1121/1.1554694.
[32] N. Guo, P. Cawley, The interaction of Lamb waves with delaminations in composite plates, J. Acoust. Soc. Am. 94 (4) (1993) 2240–2246, https://doi.org/10.1121/1.407495.
[33] R. Courant, K. Friedrichs, H. Lewy, On the partial difference equations of mathematical physics, IBM J. Res. Dev. 11 (2) (1967) 215–234, https://doi.org/10.1147/rd.112.0215.
[34] F.P. Beer, E.R. Johnston Jr., J.T. Dewolf, Mechanics of Materials, third ed., McGraw-Hill, 2001.
[35] V. Giurgiutiu, Electroactive and magnetoactive materials, in: V. Giurgiutiu (Ed.), Structural Health Monitoring with Piezoelectric Wafer Active Sensors, second ed., Academic Press – Elsevier, 2014 https://doi.org/10.1016/C2013-0-00155-7.
[36] N. Pérez, F. Buiochi, M.A.B. Andrade, J.C. Adamowski, Numerical characterization of soft piezoelectric ceramics, AIP Conf Proc 1433 (2012) 648–651, https://doi.org/10.1063/1.3703267.
[37] J.H. Nieuwenhuis, J.J. Neumann, D.W. Greve, I.J. Oppenheim, Generation and detection of guided waves using PZT wafer transducers, IEEE Trans. Ultrason. Ferroelectrics Freq. Contr. 52 (11) (2005) 2103–2111, https://doi.org/10.1109/TUFFC.2005.1561681.
[38] P.A. Viegas Ochôa de Carvalho, Supporting Data for Finite-Element Simulations of Ultrasonic Guided Wave Propagation on a Plate with a Permanently Corrugated Shape, 4TU.Centre for Research Data, 2019. http://doi.org/10.4121/uuid:faa62d35-1444-4e40-a970-404c2b0c83cd.